



HAL
open science

Combined angular and energy dispersive diffraction: optimized data acquisition, normalization and reduction

A King, N Guignot, L Henry, G Morard, A Clark, Y Le Godec, J-P Itié

► To cite this version:

A King, N Guignot, L Henry, G Morard, A Clark, et al.. Combined angular and energy dispersive diffraction: optimized data acquisition, normalization and reduction. *Journal of Applied Crystallography*, 2022, 55, pp.218 - 227. 10.1107/s1600576722000322 . hal-03853157

HAL Id: hal-03853157

<https://hal.science/hal-03853157>

Submitted on 15 Nov 2022

HAL is a multi-disciplinary open access archive for the deposit and dissemination of scientific research documents, whether they are published or not. The documents may come from teaching and research institutions in France or abroad, or from public or private research centers.

L'archive ouverte pluridisciplinaire **HAL**, est destinée au dépôt et à la diffusion de documents scientifiques de niveau recherche, publiés ou non, émanant des établissements d'enseignement et de recherche français ou étrangers, des laboratoires publics ou privés.



Combined angular and energy dispersive diffraction: optimized data acquisition, normalization and reduction

A. King,^{a*} N. Guignot,^a L. Henry,^a G. Morard,^{b,c} A. Clark,^{d,e} Y. Le Godec^e and J.-P. Itié^a

Received 4 November 2021

Accepted 10 January 2022

Edited by A. Borbély, Ecole National Supérieure des Mines, Saint-Etienne, France

Keywords: X-ray diffraction; synchrotron; liquid structures; amorphous structures.

^aPSICHE Beamline, Synchrotron SOLEIL, L'Orme des Merisiers, 91192 Gif-sur-Yvette, France, ^bUniversité Grenoble Alpes, CNRS, IRD, IFTTAR, ISTerre, 38000 Grenoble, France, ^cIMPMC, UMR CNRS 7590, Sorbonne Universités, Paris, France, ^dGeological Sciences, University of Colorado, Boulder, CO 80309-0399, USA, and ^eIMPMC, UMR CNRS 7590, Sorbonne Universités, MNHN, Paris, France. *Correspondence e-mail: king@synchrotron-soleil.fr

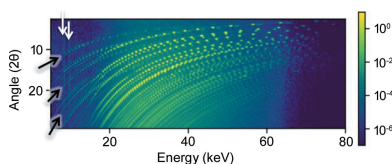
Combined angular and energy dispersive diffraction is particularly well suited to experiments at high pressures in large-volume presses, and to the study of liquid or amorphous systems. This work describes the data acquisition, correction and reduction approach developed at the PSICHE beamline of the SOLEIL synchrotron. The measured data were normalized for both the scattering volume and the effective incident energy spectrum. By optimizing the acquisition strategy, the measurement time and radiation dose are greatly reduced. The correction and reduction protocol outputs normalized scattering profiles that are suitable for pair distribution function or liquid structure analysis. These processes are demonstrated with examples from a number of real experimental data sets.

1. Introduction

Synchrotron X-ray diffraction uses the signal of radiation scattered from the atoms of a sample. Two experimental configurations can be considered. The more commonly used method is angular dispersive diffraction. In this case, a monochromatic X-ray beam is incident on the sample. The X-rays are scattered by the sample, and the experiment measures the distribution of scattered intensity as a function of the angle. The second method is energy dispersive X-ray diffraction (EDX). In this case, a polychromatic X-ray beam is incident on the sample. A particular diffraction angle is defined, and the energy spectrum of the X-rays scattered at this angle is measured. Various techniques exist combining these two concepts. Here we describe an optimized data acquisition, correction and reduction approach developed at the PSICHE beamline of the SOLEIL synchrotron.

1.1. Energy dispersive diffraction

An EDX experiment uses a polychromatic X-ray beam. A first set of slits (s_1) is used to define the incident beam. An energy-sensitive point detector is used to record a diffraction spectrum. The diffraction angle is chosen using two sets of slits between the sample and the detector (w_1 and w_2). The intersection of the beams defined by the incident and the detector slits describes a gauge volume, from which the diffracted signal is measured, as shown schematically in Fig. 1. Materials outside this gauge volume do not contribute directly to the measured signal, so the signal of the sample is separated from its environment. This is important for high-pressure experiments in large-volume presses, where the sample is



surrounded by a confining assembly. It is also useful in engineering or cultural heritage contexts, because it allows a diffraction measurement to be obtained from a precise location within a larger sample. Because the detector is energy sensitive, X-ray fluorescence peaks can be observed superimposed on the diffraction spectrum. This may hinder diffraction analysis but can be a useful tool for detecting the presence of certain elements (King *et al.*, 2019; Dik *et al.*, 2008; Gregoire *et al.*, 2009). EDX also has certain limitations compared with an angular dispersive measurement. The reciprocal space coverage is reduced, restricted to a single detector element in most cases, although multi-detector designs do exist (Drakopoulos *et al.*, 2015; Steuwer *et al.*, 2010). The PSICHE instrument is equipped with a seven-element detector covering about 70 mm. The inherent peak width is generally larger than that in a monochromatic synchrotron measurement, as the counting statistics of the detector impose a minimum resolution (typically 120–260 eV in the 20–100 keV range). Energy-resolving detectors also have a limited maximum count rate that must be respected. The XIA FalconX system used at PSICHE has a maximum count rate of 4×10^6 counts per second (<https://xia.com/FalconX.html>). In service, we typically aim to avoid exceeding 2×10^5 counts per second per channel. This typically corresponds to a dead time (time when the detector cannot receive the signal because the electronics are busy) of less than 20%. Finally, the Q range of a single measurement is limited by the spectral range of the incident beam, and the observed diffracted intensities are a function of this spectrum. If we consider the PSICHE beam-

line, with a white beam spectrum from around 20 to 80 keV, d spacings from 1.3 to 4.4 Å are accessible in a single acquisition at 8° (2θ).

1.2. Multi-angle energy dispersive X-ray diffraction

A number of researchers have used multi-angle energy dispersive data acquisitions for the study of liquid or amorphous samples (Kono *et al.*, 2018; Sato *et al.*, 2010; Yamada *et al.*, 2011; Funamori *et al.*, 2004; Sanloup & de Grouchy, 2018). Here, the motivation to use EDX is that the spatially defined gauge volume allows the signal from the sample to be distinguished from the surrounding sample environment and that a large Q range can be accessed. In the case of PSICHE, extending the 2θ range from 2.5 to 29.5° means that d spacings from 0.3 to 9.5 Å are accessible. In a multi-angle acquisition, a few energy dispersive spectra are measured, covering a wide angular range with a large step size (*e.g.* $3 < 2\theta < 37^\circ$, with 2θ steps of $3\text{--}7^\circ$). The profiles are normalized by an effective incident intensity and combined to form one profile with an extended Q range. Determining the appropriate energy spectrum $[I_{\text{eff}}(E)]$ for normalization is not straightforward, as it is dependent on the sample and sample environment due to beam hardening (Yamada *et al.*, 2011). Combining the spectra into a single profile may require additional empirical normalization factors to correct for the changing geometry.

1.3. CAESAR concept

The combined angular and energy dispersive structural analysis and refinement technique (CAESAR) was first described by Wang *et al.* (2004) and is designed to overcome some of the limitations of a standard EDX system. The energy dispersive detector is mounted on a rotation stage, which allows the diffraction angle to be changed while maintaining the alignment of the incident and diffracted beams at the same point (Fig. 1). A CAESAR acquisition consists of a series of EDX spectra, acquired from the same point in the sample. Each detector channel effectively produces a monochromatic, angular dispersive spectrum. Wang *et al.* (2004) describe how, for a small range of energies around a chosen energy, the variation in the incident beam spectrum can be considered negligible and no normalization is required. The effective angles of these data points can be calculated to provide more data points for an angular dispersive profile. These fill in the gaps between the angular steps. Thus, relatively coarse angular stepping (0.1° in 2θ is suggested) can be used while maintaining a good effective angular resolution. Note that the peak width is still dominated by the resolution of the EDX detector. Although limited, the energy bandwidth used is much greater than the bandpass of a monochromator, and hence the measurement is faster than scanning with a monochromatic beam. The total energy range accessible may also exceed what a standard monochromator can select. The range of angles means that a greater d -spacing range is accessible.

1.4. Optimized CAESAR acquisition and analysis

The strategy presented here combines features of the above approaches. We aim to use as much of the beam spectrum as

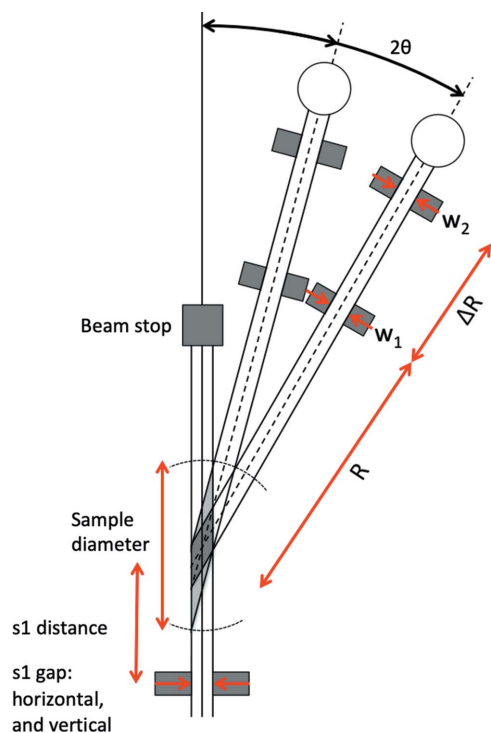


Figure 1
Schematic geometry of the CAESAR instrument. The detector moves to cover a range of 2θ angles (Wang *et al.*, 2004). Two intermediate angular positions are shown.

possible, combined with the full angular scan range. This provides the maximum Q range with the optimal acquisition time and signal-to-noise ratio. Using a larger step size than a classical CAESAR acquisition (typically 0.2°) keeps the total time reasonable, while allowing rebinning-type approaches to be exploited if desired. The redundant data are used to calculate the effective incident spectrum and geometrical corrections for normalization. The acquisition is managed such that the detector count rate is optimal at all angles. In this paper we describe the acquisition and analysis routines implemented at the PSICHE beamline to achieve these goals.

2. Optimized data acquisition

As stated above, solid-state germanium detectors have a limited maximum count rate. Exceeding this rate will result in excessive dead time and artefacts in the data. However, if the diffraction signal is too small, counting times will become excessively long and the signal-to-noise ratio will be poor. The scattering power of materials drops rapidly as a function of angle. The size of the diffraction gauge volume depends on the slit gaps and diffraction angle. The rigorous calculation of gauge volume is crucial to this work and is described in Appendix A. The aim of an optimized CAESAR acquisition is to keep the detector count rate high at all diffraction angles, whilst not exceeding a predetermined maximum.

It is considered preferable to minimize the X-ray dose on the sample to avoid beam damage and minimize noise, and hence it is better to increase the count rate by opening the detector slits (w_1 and w_2) rather than the incident slits. With a sample–detector distance greater than 1 m and a w_2 slit opening of a few millimetres, the angular resolution of the detector is generally insignificant compared with the energy resolution ($\Delta E/E \simeq 5 \times 10^{-3}$ at 40 keV). As a result, opening the detector slits does not degrade the instrumental resolution. In general, the detector slits are fully open in the vertical direction to maximize both efficiency and reciprocal space coverage. The vertical dimension of the gauge volume is constant and defined by the incident slits. Vertical focusing using a curved mirror may be used to increase the flux density in the white beam. In this case the angle of incidence is adjusted such that all desired energies are reflected, avoiding the low pass filter effect described by King *et al.* (2016). The counting time can be adjusted as a function of angle to further improve the signal-to-noise ratio at high angles. Wang *et al.* (2004) progressively opened the incident beam vertical slit gap to obtain a reasonably constant count rate. This is easier in terms of data analysis but increases the X-ray dose and may not be possible in the case of small samples or restricted access. Similarly, Yamada *et al.* (2011) described changing the slit gaps at different angles, without specifying which are adjusted.

The acquisition strategy is defined prior to data collection. A number of constraints and geometry parameters are set. Typical values used at PSICHE are shown in Table 1 (see Fig. 1 for definitions).

We first define a fixed, optimum ratio between the detector slit gaps (w_1 , w_2) based on the instrument geometry (see

Table 1
Acquisition parameters and typical values.

Acquisition parameter	Typical value
Start angle 2θ	2.5°
End angle 2θ	29.5°
2θ step	0.2°
Incident slit gap	0.025 mm
Minimum (starting) w_1 gap	0.035 mm
Maximum allowed w_2 gap	2 mm
Counting time low angles ($<12^\circ$)	3 s
Counting time medium angles ($\geq 12^\circ$, $<20^\circ$)	6 s
Counting time high angles ($\geq 20^\circ$)	12 s
Sample diameter/thickness	2 mm
Incident slit s1 to sample distance	470 mm
Sample to w_1 detector slit distance (R)	250 mm
w_1 to w_2 detector slit distance (ΔR)	970 mm
Instrument beam divergence (effective X-ray source size and source to s1 distance)	0.9 mm FWHM at 24 m

Appendix A). We then define the incident s1 slit gap and the initial w_1 slit gap that will be used at the lowest angle. The integral signal is calculated from the intersection of the gauge volume with the sample diameter and the angular opening of the detector. An iterative routine seeks to achieve a constant signal at all angles. The horizontal detector slit gaps are adjusted, while the incident slits are kept constant. The algorithm can be adapted to adjust other parameters or to optimize other criteria, for example to ensure that the gauge length does not exceed the sample diameter.

After this calculation, the user has the option of further opening the detector slits at high angles to compensate for the reduction in scattering power with angle and maintain the detector count rate. Given the typical beam spectrum of the PSICHE beamline (maximum flux around 25–35 keV depending on sample attenuation), we typically observe the highest detected count rates around $8\text{--}10^\circ$ 2θ (corresponding to a d spacing of about $2\text{--}3 \text{ \AA}$ at 30 keV). This ‘boost’ strategy is an empirical adjustment, which opens the detector slits after 10° by a factor of $1 + (2\theta - 10) \times 0.15$, corresponding to a factor of 4 at 30° . This means that the gauge is $4\times$ longer and the angular opening is $4\times$ greater, giving $16\times$ greater signal. Note that the gauge length at higher angles is generally much smaller than that at low angles [because of the factor of $1/\sin(2\theta)$] so this increase does not result in an excessive gauge length. For other beamlines with different beam spectra this empirical adjustment can be adapted accordingly. Finally, longer counting times are used at higher angles to further reinforce the weaker scattering signals.

If a naïve acquisition strategy with constant slit gaps and counting times is used, the gauge volume is reduced by approximately a factor of 10 from 2.5 to 29.5° , and the angular opening remains constant. In the optimized scan, the integrated signal remains constant, or if the ‘boost’ is used, it increases by a factor of $16\times$. Including the effect of using shorter counting times at low angles, the total acquisition time is around $15\times$ faster than a non-optimized case. A full CAESAR acquisition thus requires about 20 min or less, rather than 8 h. In practice, the benefit is actually more important, because if there is a certain level of background

noise the weak signals at high angles may be impossible to measure. Shorter acquisition times are of crucial importance when studying liquid samples at high pressures and temperatures due to the difficulty of maintaining the desired experimental conditions.

The data are automatically acquired according to the chosen strategy, and are saved together with the instrument geometry and scanning parameters. The detector ‘live time’ and ‘real time’ are recorded for each step. The difference between the two is the dead time, related to the time lost whilst the detecting system processes each event. This dead time increases with the input count rate.

3. Data analysis

Data analysis and display is performed using Python routines. Only commonly used libraries are required, making installation simple. The source code is available from GitLab: <https://gitlab.com/soleil-psiche/caesardata.git>.

3.1. Conversion

The CAESAR data are recorded in the form of a 2D array of energy and angle, with a possible third dimension if the detector has multiple elements $I_{\text{obs}}(E, 2\theta, [\text{element}])$

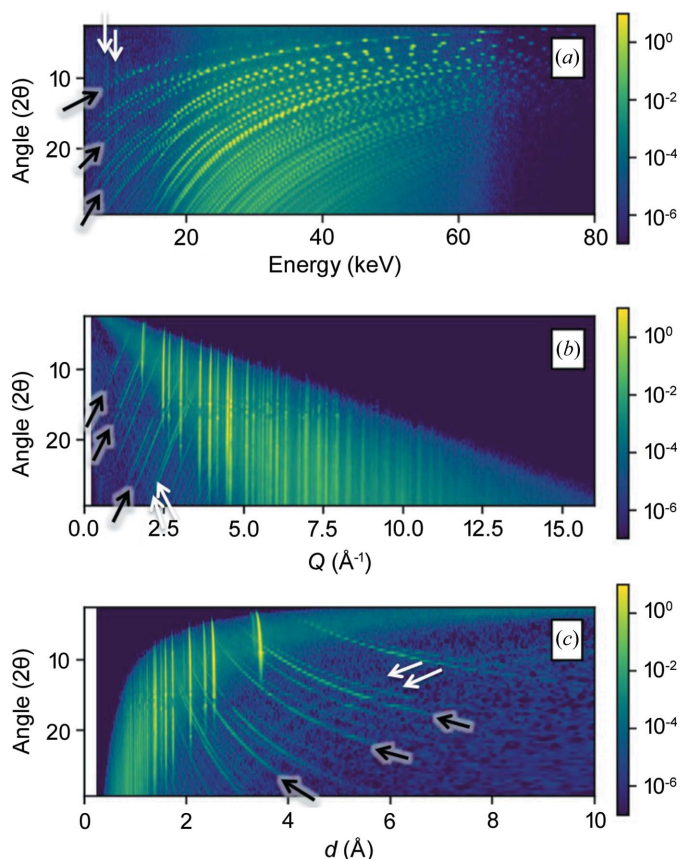


Figure 2 CAESAR acquisition from crystalline alumina powder (Al_2O_3). Conversion between (a) $I(E, 2\theta)$, (b) $I(Q, 2\theta)$ and (c) $I(d, 2\theta)$. Note the germanium fluorescence peaks (white arrows) and escape peaks (black arrows). The diffraction lines appear ‘spotty’ in (a) because of the angular step size. Logarithmic scale.

[Fig. 2(a)]. Necessary for this work is the concept of transforming this array into $I_{\text{obs}}(Q, 2\theta, [\text{element}])$ or $I_{\text{obs}}(d \text{ spacing}, 2\theta, [\text{element}])$, as shown in Fig. 2. Linear interpolation is applied to each EDX spectrum to produce a new array in the desired units.

3.2. Binning

For liquid or amorphous materials, the non-crystalline diffraction signal is typically rather smooth and slowly varying. In this case the data can be rebinned by a factor of two or four to create wider energy bins, with a corresponding improvement in the signal-to-noise ratio. The intrinsic energy resolution of the detector may also justify the use of this step for crystalline materials.

3.3. Background correction

As described by Yamada *et al.* (2011), background correction is often unnecessary due to the well collimated beams and defined gauge volume. If the sample is much smaller than the gauge volume, or the material around the sample is strongly scattering, an acquisition from an empty cell or sample holder using the same conditions may be subtracted as a first step.

3.4. Corrections: escape peaks

Energy dispersive detectors are affected by the phenomena of escape peaks. The energy of an absorbed X-ray photon generates electron–hole pairs in the germanium, which are counted to determine the photon energy. However, in some cases, the X-ray photon causes the photoelectric ejection of an electron, which requires 9.88 keV, and only the remaining energy generates electron–hole pairs. The counted electron–hole pairs therefore underestimate the photon energy by 9.88 keV. This produces spurious peaks in the data, known as escape peaks, which are evident when viewed in a 2D CAESAR data set (Wang *et al.*, 2004) since they do not exhibit the Bragg law behaviour of diffraction peaks. Note that fluorescence peaks show a different, non-Bragg law behaviour (Fig. 2). Fig. 3 shows part of an acquisition prior to correction. The effect is strongest close to the excitation energy and becomes negligible at higher energies (<1% at 44 keV). Data are corrected as follows. A CAESAR acquisition was performed on a crystalline powder sample of alumina (Al_2O_3), shown in Fig. 2. The data were treated as a series of EDX spectra. All peaks were fitted and pairs of peaks separated by 9.88 keV identified. The relative intensities of these peaks were used to relate the intensity of the escape peak [$I^*(E - 9.88)$] to the intensity of the true peak [$I(E)$], as a function of energy. An exponential function was fitted to these data:

$$I^*(E - 9.88) = I(E) \times 0.415 \exp(-0.0854E). \quad (1)$$

The data are corrected in two steps. First, the measured profile is multiplied by the exponential function to determine the escape peak intensity. This intensity is subtracted from the escape peaks (at $E - 9.88$). The profile is multiplied by the exponential function a second time to estimate the missing

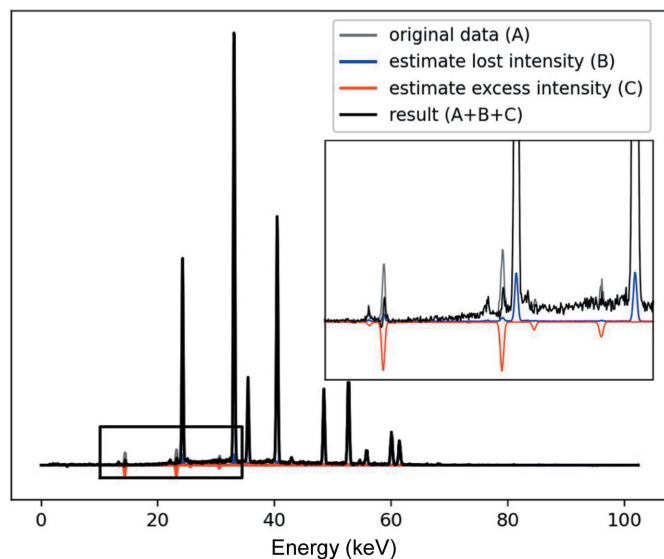


Figure 3
Escape peak correction. The profile shown is extracted from the crystalline alumina powder data set shown in Fig. 2.

intensity, which is added to the real peaks (at E). This simple correction neglects second-order effects (doubly escaped peaks, effects due to overlapping real and escape peaks, $K\alpha_2$ escape peaks). The effect of the correction is shown in Fig. 3.

3.5. Corrections: remove spurious peaks

For amorphous or liquid samples, it may be necessary to apply a second correction to remove unwanted diffraction peaks from crystalline materials in or around the sample. In this case, the 2D nature of the CAESAR data set is exploited. This allows a large body of image correction techniques to be used. In this case, a modified 2D median filter is used (Arce *et al.*, 2005). Such filters are particularly effective in removing ‘salt and pepper’ noise. To avoid modifying the data set more than necessary, the behaviour of this filter is modified to ensure that it only reduces high values but does not increase local minima by taking the pixelwise minimum of original and filtered images. The size of the filter kernel is adjusted to suit the data set. As an alternative to filtering, masking can be used to remove problematic local regions of the image (shadowed areas, strong fluorescence signals) without modifying the rest of the data. Masks can be defined manually or can be generated using an image analysis approach. Masked regions are ignored in the subsequent treatment.

3.6. Pre-normalization

The initial data analysis step is a pre-normalization of the data. This uses the detector live time to convert the spectra from total counts [Fig. 4(a)] to counts per second [Fig. 4(b)]. The gauge volume and the angular opening of the detector are calculated for each angle as described in Appendix A and used to prenormalize the spectra [Fig. 4(c)]. This removes the obvious steps associated with different counting times and corrects for the changing gauge volume as a function of the angle.

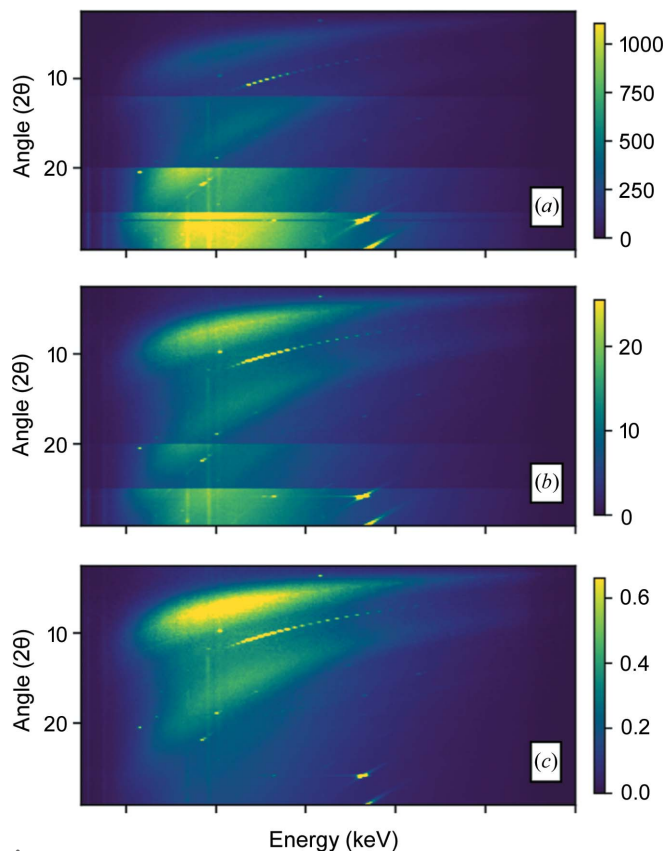


Figure 4
CAESAR data from an amorphous MgSiO_3 sample, at ambient temperature and pressure but in a Paris–Edinburgh assembly. (a) Recorded data (counts), (b) corrected for live time (counts per second), (c) prenormalized for volume and detector angular opening (AU).

3.7. Normalization

The intensities observed in each energy dispersive spectrum are dependent on the incident polychromatic beam spectrum, the attenuation of the beam by the sample and surrounding materials, and the response of the detector. To combine the 2D CAESAR acquisition into a single profile, it is necessary to normalize the data by this spectrum, referred to by Yamada *et al.* (2011) as the effective source intensity, $I_{\text{eff}}(E)$. This can be calculated if the instrument spectrum and the filtering effect of the sample are known. It may be possible to use the air scattering signal after the sample; however, this is an approximation because low energies are scattered more effectively by air. Alternatively, the diffracted signal at high angles may be used as an approximation (*e.g.* Funamori *et al.*, 2004). Note that the effective source intensity may change from one measurement to another due to changes in the thickness or composition of the sample modifying the attenuation of the beam. Here we describe a novel method for determining the effective spectrum for amorphous or liquid samples.

We propose an iterative routine, inspired by the work of Funakoshi (1997). Upper and lower energy bounds are selected, in order to keep only those data where the signal-to-noise ratio is judged acceptable. The calculation of the effective spectrum is based on the principle that, if the data are normalized by the correct spectrum, the redundant data

(measurements at the same Q , for different E and 2θ) will be consistent. Data are prenormalized and artefacts corrected, as described above. The first step is to calculate the value of Q for

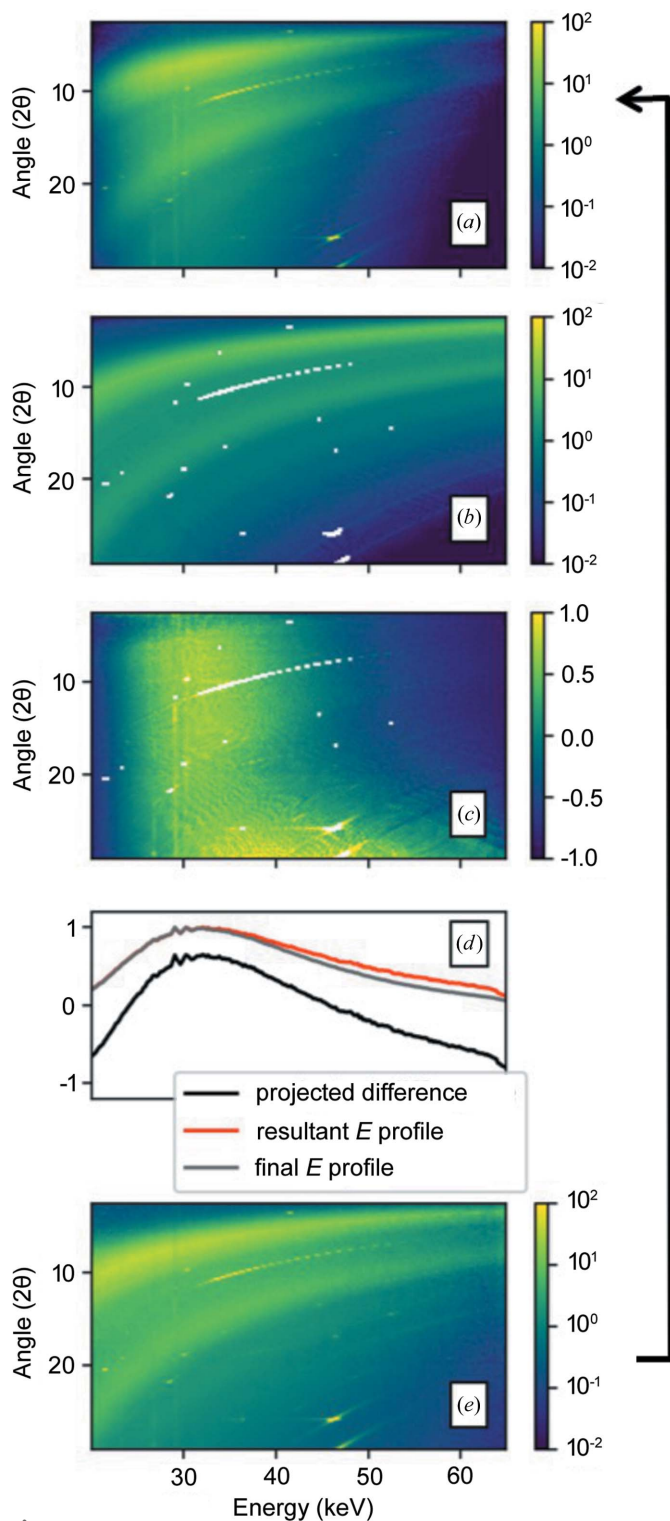


Figure 5 Iterative normalization steps applied to the amorphous MgSiO_3 data set. (a) $I_{\text{norm}}(E, 2\theta)$ at iteration 0. (b) Average intensity along equal Q values. Note the masking of crystalline peaks in this amorphous sample (white). (c) Difference. (d) Project the average difference onto E or 2θ , and use to adjust I_{eff} and/or k . (e) Apply this to generate $I_{\text{norm}}(E, 2\theta)$ iteration 1.

every data point of the 2D or 3D matrix of data. Thus, for every point we have an energy, an angle and a Q value. Any masked points are simply ignored in subsequent calculations. We can create 1D profiles by grouping data points into bins according to their E , 2θ or Q values, and averaging the values together. For each bin, we can exclude outliers by including only those values within a certain number of standard deviations from the mean. For computational efficiency, prior to the iterative calculation a series of tables are created assigning data points to bins in E , 2θ and Q .

We aim to calculate two functions: $I_{\text{eff}}(E)$ and $k(2\theta)$. The second function is a correction to the prenormalization. Both functions are initialized with uniform values.

3.8. Algorithm

Normalize the data set:

$$I_{\text{norm}}(E, 2\theta, \text{channel}) = \frac{I_{\text{obs}}(E, 2\theta, \text{channel})}{I_{\text{eff},0}(E) k(2\theta)}. \quad (2)$$

Compute a guess of $I(Q)$, by taking the mean of all data points with similar Q values.

Calculate the difference of each data point from the profile $\text{dif}(E, 2\theta, \text{channel})$.

Create the average difference as a function of E and/or 2θ , excluding outliers.

Apply this difference to the $I_{\text{eff}}(E)$ and $k(2\theta)$ profiles.

Iterate.

These steps are illustrated in Figs. 5(a)–5(e). This function usually converges within fewer than ten iterations. As a default strategy, we apply three iterations in which only $I_{\text{eff}}(E)$ is adjusted. Then, both $I_{\text{eff}}(E)$ and $k(2\theta)$ are allowed to vary. The standard deviation of the difference values is used to monitor convergence and stop the iteration when the change is less than a predefined value. Fig. 6 compares the prenormalized

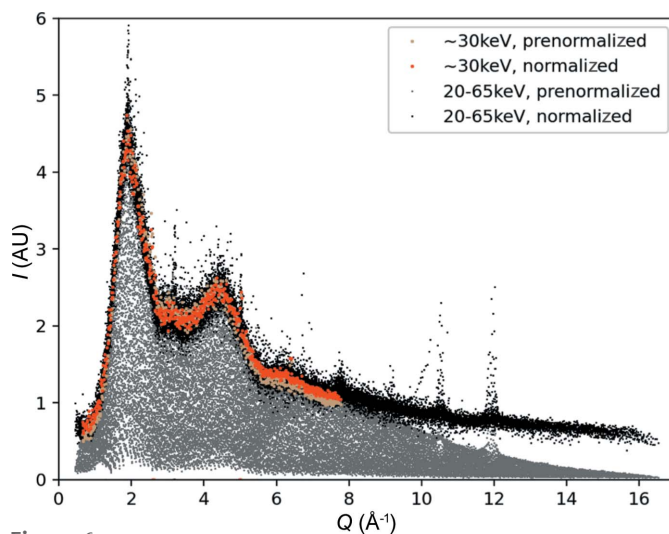


Figure 6 Comparison between data before and after iterative normalization. Shown are all data between 20 and 65 keV, and those data points for 30 ± 0.5 keV. Data points that are masked in Fig. 5 are shown but were not used in the normalization.

and final normalized data, demonstrating how, after normalization, all data points fall onto a single profile.

Amorphous samples produce smooth diffraction patterns due to the absence of grain sampling effects, and therefore very consistent intensity for a given Q value. Crystalline samples exhibit sharp diffraction peaks, and for most real materials the peak intensities are strongly modified by grain-sampling statistics. This can be seen in Fig. 2(b) from an alumina powder sample. Despite a fine grain size, some intensity variations are observed. However, with appropriate masking or outlier exclusion during the iterative calculation, a reasonable normalization can be obtained.

3.9. Data around the tungsten K edge

It has been observed that there may be problems with achieving reliable normalization of the data in the vicinity of the tungsten K edge, located at 69.5 keV. In some cases, it is necessary to limit the maximum energy used to below this edge. This is often the case in our data but is also evident in other work (Sato *et al.*, 2010; Yamada *et al.*, 2011). Here we attempt to explain this problem by considering the transmission through the edges of the beam-defining slits. The slits used at PSICHE have tungsten carbide blades, with 4 mm thickness and a 0.5° knife-edge angle (<https://www.jjxray.dk>). Therefore, with a parallel beam and perfectly aligned slits, there exists a $35\ \mu\text{m}$ zone where the projected thickness of the slit blade varies linearly between 0 and 4 mm. Any misalignment of the slit blades, and the divergence of the beam, will enhance this effect. Intensity transmitted through the thinner material will effectively increase the slit opening, hence increasing the gauge volume and the angular opening, creating

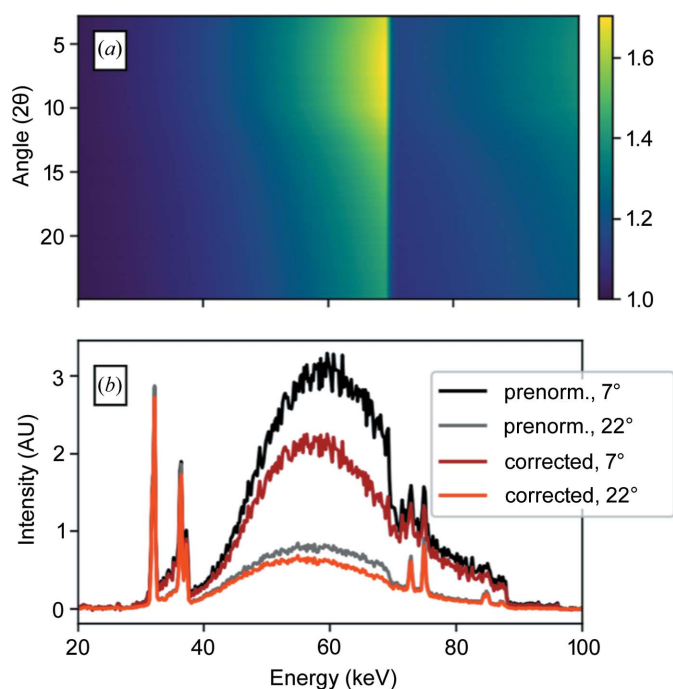


Figure 7
Slit gap correction. (a) Ratio of excess intensity due to slit edges, 4° misalignment. (b) Effect of this correction on energy dispersive profiles from a lead glass data set.

extra signal. As the attenuation coefficient of the slit material varies with energy, these effects are energy dependent. The excess signal increases progressively with energy and is largest just below the K edge, before dropping suddenly after the edge. The extra slit opening is a constant offset and therefore has a stronger impact when the slit gaps are smallest. With our optimized acquisition strategy, this occurs at low diffraction angles.

Without correction, this effect is visible in the data as an excess of intensity below the W K edge. Using the tools for normalizing CAESAR data, we can attempt to correct for the effective slit gap. Assuming a constant misalignment on all slits, we can calculate the effective additional slit opening as a function of energy. Then we can calculate a correction factor for each energy and for the instrument geometry at each angle. When applied to a data set exhibiting the problem, this removes the step in intensity at the tungsten edge, as shown in Fig. 7. If this is not corrected, the iterative normalization procedure will attempt to account for the excess intensity by adjusting $I_{\text{eff}}(E)$ and $k(2\theta)$, but cannot succeed perfectly because the effect depends simultaneously on the energy and angle. It may be possible to reduce this effect using slits with a large-radius cylindrical edge profile.

4. Results

Fig. 8 shows the results of applying the method described to an amorphous MgSiO_3 sample. The sample was measured under

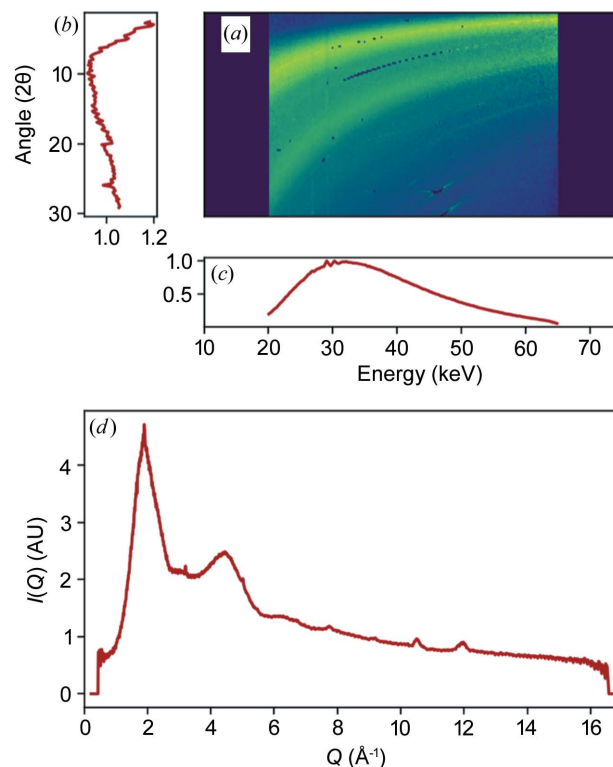


Figure 8
(a) Normalized CAESAR acquisition from amorphous MgSiO_3 . (b) Calculated correction to prenormalization. (c) Calculated $I_{\text{eff}}(E)$. (d) Resultant $I(Q)$ profile for this acquisition.

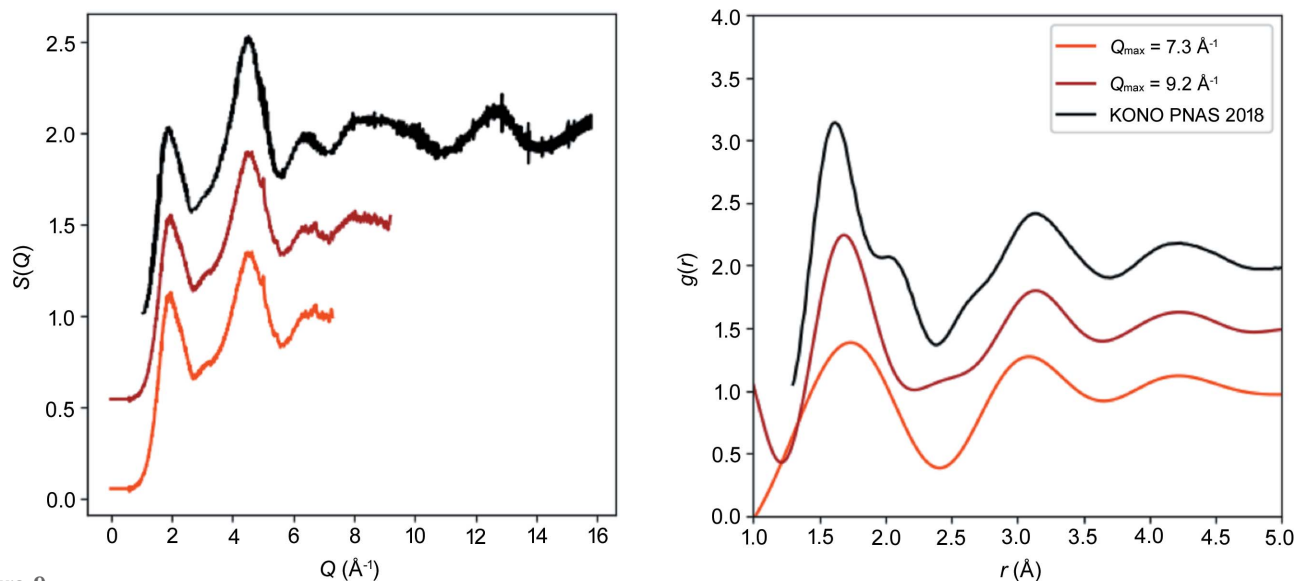


Figure 9 $I(Q)$ and $g(r)$ for the amorphous MgSiO_3 presented in Fig. 8, determined for two values of Q_{max} . The results are compared with the work of Kono *et al.* (2018).

ambient conditions but in a Paris–Edinburgh assembly. The acquisition covers $2.5\text{--}29.1^\circ$ in 2θ , using geometry parameters similar to the typical values in Table 1. The data have been normalized over an energy range from 20 to 65 keV. The acquisition time was around 100 min with a single-element Ge detector. With the new seven-element detector, a data set with a similar signal-to-noise ratio could be acquired in less than 10 min, due to multiple detector elements and a higher maximum count rate. The calculated w profile extends from >1 to $>15 \text{ \AA}^{-1}$.

These data have been converted to $S(Q)$ and $g(r)$ with the *Amorpheus* software package (Boccatto *et al.*, 2021), using two different values of Q_{max} , 7.3 and 9.2 \AA^{-1} . The resultant profiles are shown in Fig. 9, compared with the work of Kono *et al.* (2018). The profiles show very good agreement, demonstrating the validity of our normalization approach. We note that, in the article from which the comparison is drawn, acquisition times are stated to be between 3 and 5 h (Kono *et al.*, 2018). Because our data were acquired in an assembly and press, they correspond more closely to the high-pressure measurements of Kono *et al.* (2018). These had a Q_{max} of 13 \AA^{-1} and were not able to resolve the shoulder to the first peak of the $g(r)$ at around 2 \AA . Collecting data to the highest possible Q_{max} is of great importance in order to obtain the best possible profiles of $g(r)$. In the present case, the Q_{max} in our data is somewhat limited because of the requirement to minimize the acquisition time. The maximum accessible Q value of a CAESAR acquisition at the PSICHE beamline is in the range $15\text{--}20 \text{ \AA}^{-1}$, corresponding to an energy of $\sim 75 \text{ keV}$ and 2θ of 30° .

5. Conclusions

We have demonstrated an optimized acquisition strategy for CAESAR experiments. This reduces the measurement time by a factor of more than ten, to the order of tens of minutes.

Even shorter acquisition times are achievable with strongly scattering samples. This enables studies of evolving systems, or the possibility of making multiple repeat measurements in an inhomogeneous sample. The speed of acquisition is particularly important for the study of liquids at high pressure and temperature, where it may not be possible to maintain the conditions for long durations. At the same time, the radiation dose applied to the sample is also minimized. Finally, by maximizing the signal-to-noise ratio at high angles, we are able to access exploitable high- Q data from weakly scattering samples.

We have presented the data-treatment strategy implemented to produce normalized profiles of scattered intensity as a function of Q over an extended Q range. This has been implemented for amorphous materials but is also applicable to polycrystalline samples. This normalization algorithm exploits the large amount of redundant data in a CAESAR acquisition to calculate $I_{\text{eff}}(E)$ and to correct the prenormalization of the data. An important advantage of the method is that, in most cases, no extra measurement is required, only the acquisition from the sample. Therefore any changes in the sample or sample assembly are automatically accounted for, and no extra measurement time is required.

APPENDIX A Scattering volume geometry

This is a 2D analytical calculation. In the vertical direction, it is assumed that the vertical dimension of the gauge volume is constant and the vertical opening of the detector is constant.

A1. Optimal cs1 and cs2 gaps

We constrain the detector slit gaps according to the following criteria, which we consider optimal (Fig. 10):

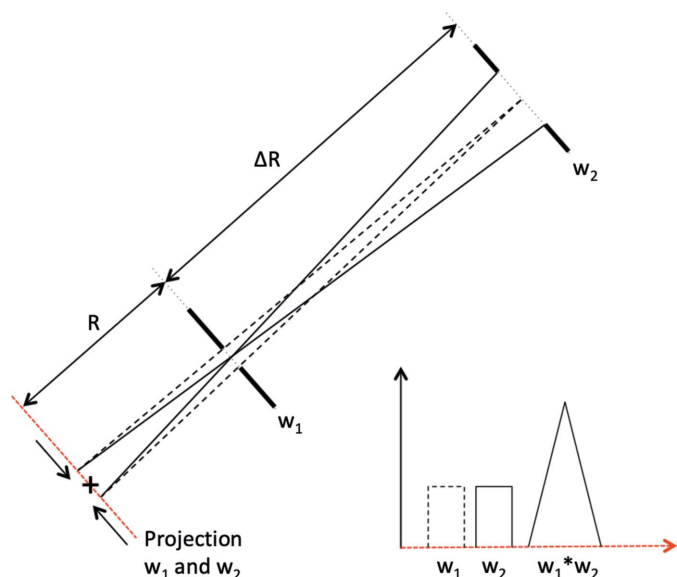


Figure 10
Optimum ratio of detector slit gaps. The projections of each slit at the gauge volume have the same width. Their convolution is a triangle.

$$w_1 \frac{R + \Delta R}{\Delta R} = w_2 \frac{R}{\Delta R} \quad (3)$$

or

$$w_2 = w_1 \frac{R + \Delta R}{\Delta R}. \quad (4)$$

This ensures that the projections of the two slit gaps at the gauge volume position are identical. This condition enforces

that the angular opening $\Delta 2\theta$, seen from the sample position, is the same for both slits. The convolution of the two equal-width boxcar functions is a triangle. This gives the greatest concentration of signal at the centre of the gauge volume. All other configurations result in a trapezoidal profile and a less localized signal.

A2. Gauge length and signal intensity

The gauge length in the primary beam direction is calculated as shown in Fig. 11. The incident beam width is given by the convolution of the synchrotron source size and the s1 slit gap, both projected onto the sample position. The integral of the incident beam contribution is normalized by the s1 slit gap, assumed to be proportional to the photon flux reaching the sample. This profile is divided by $\tan(2\theta)$ to account for the diffraction angle.

The detected beam width is given by the convolution of the two detector slits, projected onto the sample position and divided by $\sin(2\theta)$ to account for the diffraction angle. The detected beam contribution is normalized such that the peak intensity is proportional to the angular opening $\Delta 2\theta$.

The total gauge length in the beam direction is given by the convolution of the above two profiles. The total signal is given by the integral of the profile over the sample volume (from $-r$ to $+r$, where r is the sample radius). The signal is proportional to the number of incident photons, the angular opening of the detector and the volume of sample material intersecting the gauge volume, and is used for prenormalizing the measured intensity.

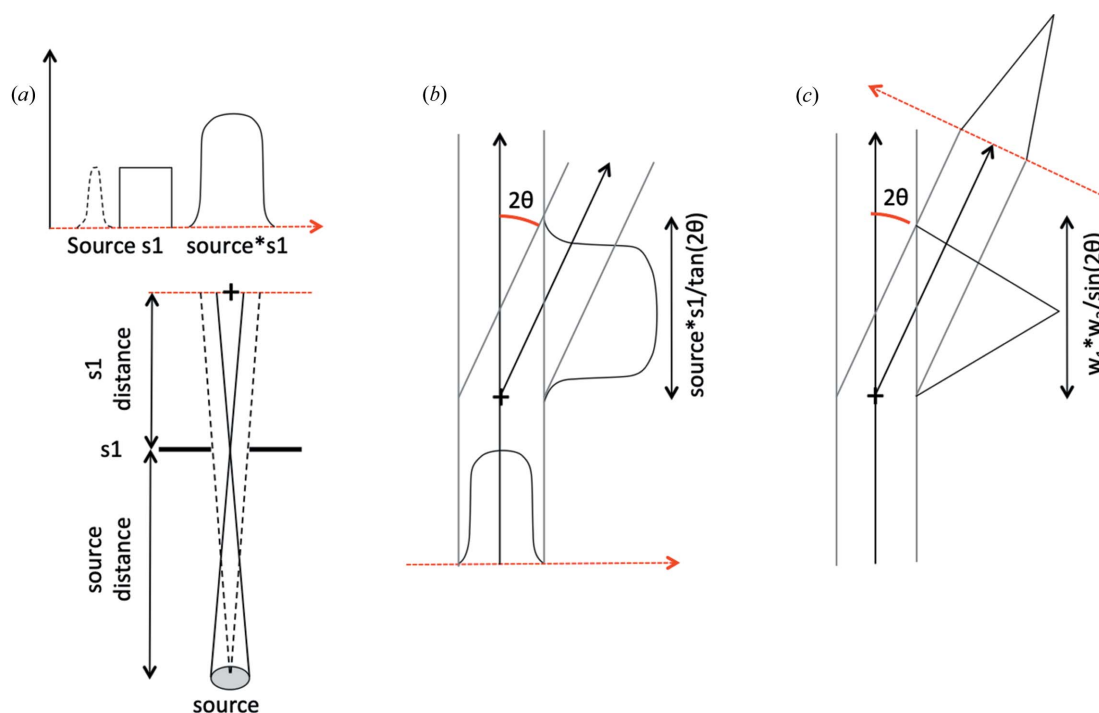


Figure 11
(a) Contribution of the source and s1 slits to the incident beam profile. (b) Contribution of the incident beam profile to the gauge length. (c) Contribution of the diffracted beam profile to the gauge length.

References

- Arce, G. R., Bacca, J. & Paredes, J. L. (2005). *Handbook of Image and Video Processing*, 2nd ed., edited by A. Bovik, pp. 109–133. Amsterdam, Boston: Elsevier Academic Press.
- Boccatto, S., Garino, Y., Morard, G., Zhao, B., Xu, F., Sanloup, C., King, A., Guignot, N., Clark, A., Garbarino, G., Morand, M. & Antonangeli, D. (2021). In preparation.
- Dik, J., Janssens, K., Van Der Snickt, G., van der Loeff, L., Rickers, K. & Cotte, M. (2008). *Anal. Chem.* **80**, 6436–6442.
- Drakopoulos, M., Connolly, T., Reinhard, C., Atwood, R., Magdysyuk, O., Vo, N., Hart, M., Connor, L., Humphreys, B., Howell, G., Davies, S., Hill, T., Wilkin, G., Pedersen, U., Foster, A., De Maio, N., Basham, M., Yuan, F. & Wanelik, K. (2015). *J. Synchrotron Rad.* **22**, 828–838.
- Funakoshi, K. (1997). PhD thesis, Tokyo Institute of Technology, Tokyo, Japan.
- Funamori, N., Yamamoto, S., Yagi, T. & Kikegawa, T. (2004). *J. Geophys. Res.* **109**, B03203.
- Gregoire, J. M., Dale, D., Kazimirov, A., DiSalvo, F. J. & van Dover, R. B. (2009). *Rev. Sci. Instrum.* **80**, 123905.
- King, A., Guignot, N., Deslandes, J.-P., Pelerin, M., Joosten, I., De Looff, D., Li, J., Bertrand, L., Rosenberg, E., Dewaele, A., Boulard, E., Le Godec, Y., Perrillat, J.-P., Giovenco, E., Morard, G., Weitkamp, T., Scheel, M., Perrin, J., Chevreaux, H. & Itié, J.-P. (2019). *Integr. Mater. Manuf. Innov.* **8**, 551–558.
- King, A., Guignot, N., Zerbino, P., Boulard, E., Desjardins, K., Bordessoule, M., Leclercq, N., Le, S., Renaud, G., Cerato, M., Bornert, M., Lenoir, N., Delzon, S., Perrillat, J.-P., Legodec, Y. & Itié, J.-P. (2016). *Rev. Sci. Instrum.* **87**, 093704.
- Kono, Y., Shibasaki, Y., Kenney-Benson, C., Wang, Y. & Shen, G. (2018). *Proc. Natl Acad. Sci. USA*, **115**, 1742–1747.
- Sanloup, C. & de Grouchy, C. (2018). *Magnas Under Pressure*, edited by Y. Kono & C. Sanloup. Amsterdam, Kidlington, Cambridge: Elsevier.
- Sato, T., Funamori, N. & Kikegawa, T. (2010). *Rev. Sci. Instrum.* **81**, 043906.
- Steuwer, A., Rahman, M., Shterenlikht, A., Fitzpatrick, M. E., Edwards, L. & Withers, P. J. (2010). *Acta Mater.* **58**, 4039–4052.
- Wang, Y., Uchida, T., Von Dreele, R., Rivers, M. L., Nishiyama, N., Funakoshi, K., Nozawa, A. & Kaneko, H. (2004). *J. Appl. Cryst.* **37**, 947–956.
- Yamada, A., Wang, Y., Inoue, T., Yang, W., Park, C., Yu, T. & Shen, G. (2011). *Rev. Sci. Instrum.* **82**, 015103.